Physics of Fluids ARTICLE scitation.org/journal/phf

Diffuse interface modeling of laser-induced nano-/micro-cavitation bubbles

Cite as: Phys. Fluids **35**, 022113 (2023); doi: 10.1063/5.0136525
Submitted: 26 November 2022 · Accepted: 1 February 2023 ·
Published Online: 23 February 2023

Dario **Abbondanza**,[1] Mirko **Gallo**,[2] and Carlo Massimo **Casciola**[1,a)]

AFFILIATIONS

[1]Department of Mechanical and Aerospace Engineering, Sapienza University of Rome, Rome, Italy
[2]Advanced Engineering Centre, School of Computing Engineering and Mathematics, Cockcroft Building, University of Brighton, Lewes Road, Brighton BN2 4GJ, United Kingdom

Note: This paper is part of the special topic, Cavitation.
[a)]**Author to whom correspondence should be addressed**: carlomassimo.casciola@uniroma1.it

ABSTRACT

In the present work, a diffuse interface model has been used to numerically investigate the laser-induced cavitation of nano-/micro-bubbles. The mesoscale approach is able to describe the cavitation process in its entirety, starting from the vapor bubble formation due to the focused laser energy deposition up to its macroscopic motion. In particular, the simulations show a complete and detailed description of the bubble formation and the subsequent breakdown wave emission with a precise estimation of the energy partition between the shock wave radiating in the liquid and the internal energy of the bubble. The scaling of the ratio between the energy stored in the bubble at its maximum radius and the one deposited by the laser is found in agreement with experimental observation on macroscopic bubbles.

I. INTRODUCTION

Cavitation and bubble dynamics have been deeply studied in the last century, both focusing on fundamental aspects and for application purposes. The qualitative picture of cavitation is well understood. Small vapor embryos can locally form in the liquid mother phase due to pressure decrease or temperature increase. Vapor nuclei, after forming, start expanding in a complex non-equilibrium process inside the mother phase. When they reach a certain maximum size, they suddenly bounce back and collapse. Bubble implosion comprises bubble topological changes, shock wave emissions, phase transition through supercritical states,[1] and intense pressure and temperature peaks, respectively.[2] Although such effects are traditionally considered to be responsible for damage on material surfaces,[3–6] cavitation is also exploited in several applications, many of which are in the field of biomedicine, such as drug delivery,[7,8] kidney stones fragmentation,[9] ophthalmic microsurgery,[10,11] and eye floaters treatment,[12] and in the field of botany.[13,14] The trend, especially in biomedicine, is to push the technological limit toward the nanoscale. For instance, near-UV laser light can be used to focus the energy deposition spot on the scale of hundreds of nanometers.[15] Although the macroscopic picture of the physical phenomenon has been well characterized, lots of questions are still open for what concerns their thermodynamics, especially when extremely small scales are involved. The crucial issue is to infer quantitative information on all the different scales of the process, which starting from the energy deposition at the nanoscale eventually involves macroscopic bubble dynamics, encompassing a wide range of scales. Since, in these conditions, experimental measurements are hard to be performed, innovative theoretical and numerical approaches are crucial. Starting from the pioneering work of Rayleigh,[16] several mathematical models have been developed to address this complex phenomenon.[17] These mathematical descriptions are based on the so-called *sharp interface* model of the liquid/vapor interface, treating the phase separation region as a mathematical discontinuity. From a mechanical point of view, the limitations of this approach emerge when the diffused nature of the liquid/vapor interface becomes important. This is the case of nanobubbles, whose size is comparable with the liquid/vapor interface thickness.[18–20] Taking into account the diffuse nature of the interface is also crucial to address bubble nucleation[21–26] and bubble collapse, where intense peaks of temperature are involved and the fluid transitions into a supercritical state.[27–29] This is what happens in one of the most effective techniques to generate controlled cavitation bubbles, i.e., the laser-induced cavitation,[30–32] in which femtosecond lasers are becoming the privileged tools for producing micro-/nanobubbles. From a qualitative standpoint, bubble generation is achieved by focusing a laser beam in a very narrow spot in a water-filled chamber. As a result, plasma is formed, and the high

energy density allows for the bubble expansion. During the bubble formation, a shock wave is emitted, the so-called breakdown shock wave, which radiates a portion of the energy deposited by the laser beam. This energy is then transformed into heat by means of thermal and viscous effects. The remaining energy is split into kinetic and internal, or potential, energy. When the bubble reaches its maximum radius, the expansion stage finishes, and the collapse stage takes place. Understanding how the energy is transformed during this process and how much is radiated by the breakdown wave and then dissipated is a difficult task, which cannot be fully solved by a purely experimental approach, due to obvious technological limitations.[30,31] In this context, the purpose of this paper is to explore the potential of numerical simulations based on a physically sound description of mesoscopic processes.

Molecular dynamics (MD) is undoubtedly an appropriate tool for the physical description of nanoscopic phenomena. However, its large computational cost makes it effectively applicable to systems of only a few tens of nanometers over nanosecond time windows.[33,34] Clearly, laser-induced micro-/nanobubbles exceed in both spatial and temporal terms its limits of applicability. One possible solution is to adopt a mesoscale description based on a diffuse interface approach.[35,36] It has already been used to describe nucleation of droplets and bubbles,[23,25,26,37] the stability limit of stretched water,[18,20] evaporation/condensation processes,[38–40] and the mechanics of lipid membranes.[41,42] In particular, the model proposed in Ref. 28 has been validated toward well-established experiments,[18] and its results are in agreement with macroscopic predictions on single bubble dynamics.[28] Here, it is exploited to address laser-induced micro-/nano-cavitation. The adopted methodology enables a robust thermodynamic description of phase change, which allows the study of bubble formation, transitions to supercritical states, and breakdown-induced shock wave formation. These intermingled processes can hardly be described by macroscopic numerical techniques, if not with the help of effective models which require the calibration of tunable parameters. To the contrary, the present model does not require any external information except the knowledge of the equation of state and transport coefficients. For this reason, the adopted model is expected to provide unprecedented high-fidelity information on the elusive process of laser-induced cavitation at the nanoscale.

II. MATHEMATICAL MODEL

The fluid description is based on the van der Waals squared gradient approximation for the Helmholtz free energy functional.[43] The approach extends the local description of a simple fluid, by including a capillary contribution that is proportional to the density gradient in the free energy,

$$F[\rho,\theta] = \int_V f_b(\rho,\theta) + \frac{\lambda}{2}\nabla\rho\cdot\nabla\rho\,\mathrm{d}V, \tag{1}$$

with $f_b(\rho,\theta)$ the bulk free energy, given in terms of mass density, ρ, and temperature, θ, fields, while λ is the capillary coefficient related to liquid/vapor interface thickness and surface tension.[28,36,44] Concerning the equilibrium properties, the van der Waals theory naturally describes the liquid/vapor coexistence, where the two phases are separated by a diffuse interface in which the physical quantities smoothly vary between the vapor and the liquid states. At constant temperature θ_0, in a closed system with a fixed volume V and mass M_0, the two phase equilibrium solution is represented by a density field $\rho_{eq}(\mathbf{x})$, which minimizes Eq. (1) with a mass constraint

$$\rho_{eq}(\mathbf{x}) = \mathrm{argmin}\left[F[\rho,\theta_0] - \mu_{ext}\left(\int_V \rho(\mathbf{x})\mathrm{d}V - M_0\right)\right], \tag{2}$$

where μ_{ext} is the equilibrium chemical potential of the system. The interface structure—$\rho_{eq}(\mathbf{x})$ the density profile at equilibrium—as provided by the theory is in good agreement with MD simulations and experiments.[18,20] In addition, the model is also able to naturally account for the surface tension, including its dependence on curvature radii (Tolman correction), capillary wave and fluctuation spectra.[45–47]

Concerning the non-equilibrium extension of the thermodynamic description, the van der Waals free-energy can be coupled with the Navier–Stokes dynamics. In this context, the evolution equations represented by the mass, momentum, and energy balances can be written as

$$\frac{\partial\rho}{\partial t} + \nabla\cdot(\rho\mathbf{u}) = 0, \tag{3a}$$

$$\frac{\partial\rho\mathbf{u}}{\partial t} + \nabla\cdot(\rho\mathbf{u}\otimes\mathbf{u}) = \nabla\cdot\mathbf{T}, \tag{3b}$$

$$\frac{\partial E}{\partial t} + \nabla\cdot(E\mathbf{u}) = \nabla\cdot(\mathbf{T}\cdot\mathbf{u}) - \nabla\cdot\mathbf{q}_e, \tag{3c}$$

with $\rho(\mathbf{x},t)$ the density, $\mathbf{u}(\mathbf{x},t)$ the velocity vector, and $E(\mathbf{x},t) = K(\rho,\mathbf{u}) + U(\rho,\theta)$ the total energy density. The latter is composed of the kinetic contribution $K = 1/2\rho\mathbf{u}\cdot\mathbf{u}$ and the internal energy $U = u_b(\rho,\theta) + \lambda/2\nabla\rho\cdot\nabla\rho$, where $u_b(\rho,\theta) = f_b - \theta\partial f_b/\partial\theta$ is the bulk contribution given in terms of density and temperature fields, once a suitable equation of state is adopted. Standard non-equilibrium thermodynamic procedure[48] allows us to identify the form of the stress tensor $\mathbf{T}(\mathbf{x},t)$ and the energy flux $\mathbf{q}_e(\mathbf{x},t)$[28]

$$\mathbf{T} = -\left(p_0 - \frac{\lambda}{2}|\nabla\rho|^2 - \rho\nabla\cdot(\lambda\nabla\rho)\right)\mathbf{I} - \lambda\nabla\rho\otimes\nabla\rho + \eta(\nabla\mathbf{u} + \nabla\mathbf{u}^T) - \tilde{\eta}\nabla\cdot\mathbf{u}\mathbf{I}, \tag{4}$$

$$\mathbf{q}_e = \lambda\rho\nabla\rho\nabla\cdot\mathbf{u} - k\nabla\theta, \tag{5}$$

where the capillary coefficient $\lambda(\theta)$ is a function of the temperature θ, η and $\tilde{\eta}$ are the first and second viscosity coefficients, respectively, and k is the thermal conductivity. In Eq. (4), the usual viscous stress tensor is augmented by distributed capillary effects concentrated in the narrow interfacial layer, and in Eq. (5), the energy flux is generalized by adding a capillary contribution to the Fourier law. System (3) is closed using the van der Waals equation of state (EoS) for the pressure $p_0(\rho,\theta)$ and the internal energy density $u(\rho,\theta)$.

In view of the law of corresponding states for the van der Waals EoS, the thermodynamic quantities p_0 and u can be reported in reduced variables, i.e., normalizing pressure, temperature, and density, with the corresponding critical values, p_c, θ_c, ρ_c, and the internal energy density with the critical pressure. Hence,

$$p_0^* = \frac{8\rho^*}{3-\rho^*}\theta^* - 3\rho^{*2} \tag{6}$$

and

$$u_b^* = 8\rho^*\theta^* - 3\rho^{*2}, \tag{7}$$

with $p_0^* = p_0/p_c$, $\theta^* = \theta/\theta_c$, $\rho^* = \rho/\rho_c$, and $u_b^* = u_b/p_c$.

III. NUMERICAL SIMULATIONS

The system of Eq. (3) has been numerically integrated to address the laser-induced bubble formation. The equations are solved in spherical coordinates by assuming the spherical symmetry of the bubble. The entire system of equations with the imposed symmetries is reported in Appendix. The initial condition is constructed in order to mimic the energy deposition of the laser inside the fluid. Clearly, the complete physical description of bubble generation by focused lasers cannot be addressed by the sole hydrodynamics equations. In fact, when the laser is focused inside the liquid, the energy input is so high as to generate ionization with subsequent plasma formation. However, it is reasonable to assume that after plasma formation, the fluid is perturbed with an energy excess consisting of the difference between the laser energy and the contribution spent in the ionization process. The localized internal energy field triggers the bubble formation through a dynamic phase change process. The specific initial conditions consist of a liquid at rest ($u_r = \mathbf{u}\cdot\hat{\mathbf{r}} = 0$, with $\hat{\mathbf{r}}$ the radial unit vector) with uniform initial liquid density. The energy spot focused in the fluid is modeled as a Gaussian function centered at $r = 0$. These conditions are represented by the following fields:

$$\rho(r,0) = \rho_l\,, \quad u_r(r,0) = 0, \tag{8}$$

$$E(r,0) = E_0 + E_{Dep}\, e^{-r^2/(2a^2)}/\sqrt{(2\pi a^2)^3}, \tag{9}$$

where ρ_l and E_0 are the initial liquid density and energy, respectively. E_{Dep} is the laser energy excess, and a^2 is the Gaussian variance related to the size of the energy spot. The equations are solved in their dimensionless form, with dimensionless parameters

$$\mathrm{Cn} = \frac{\lambda\rho_c^2}{p_c a^2} = 1.2\times10^{-4}\,, \quad \mathrm{Re} = \frac{a\sqrt{p_c\rho_c}}{\eta} = 8.35\,, \quad \mathrm{Pe} = \frac{a\sqrt{p_c\rho_c}}{k} = 1.48, \tag{10}$$

respectively, taking the place of λ, $1/\eta$, and $1/k$ in Eq. (4), where the reference values $\rho_c = 322\,\mathrm{kg/m^3}$, $p_c = 22\,\mathrm{MPa}$, $\theta_c = 647\,\mathrm{K}$, $a = 10^{-7}\,\mathrm{m}$, $v_{ref} = \sqrt{p_c/\rho_c} = 261.4\,\mathrm{m/s}$, and $t_{ref} = a/v_{ref} = 3.81\times10^{-10}\,\mathrm{s}$ have been used.

The equations have been discretized with a staggered finite difference approach on a spherical domain of extension $L = 500a$ with a uniform grid spacing $\Delta r = L/(N-1)$, and $N = 10^5$ nodal points. The evolution in time is based on an explicit second-order accurate Runge–Kutta scheme, with time step $\Delta t = 10^{-5}\, t_{ref}$.

Three initial liquid densities have been investigated, $\rho_l = 2.1$, 2.125, 2.15 (E_0 changes consequently), and, for each of them, four different values of excess laser energy in the system, E_{Dep}, have been considered.

IV. RESULTS

The overall evolution of the system is characterized by an initial violent bubble expansion, followed by successive collapses and rebounds until the bubble finally dissolves in the liquid, as shown in Fig. 1, where the radius of the liquid/vapor interface vs time is represented for different deposited energy E_{Dep} at fixed ρ_l, and the curves are normalized with the maximum bubble radius R_{max} and the time $t_{R_{\max}}$ when it is attained. For $t > t_{R_{\max}}$, the vapor bubble starts shrinking due to the pressure difference between vapor content and the surrounding liquid. As a result, the bubble is compressed up to a point where the vapor phase transitions to a supercritical state, $\theta > \theta_c$, in which it essentially behaves like a non-condensable (supercritical) fluid bubble ($t \approx 2.3 t_{R_{\max}}$). During this phase, no more vapor remains and the liquid/vapor interface $\rho = \rho_c$ ceases to be defined, see Fig. 1, to reappear during the following rebound.[27]

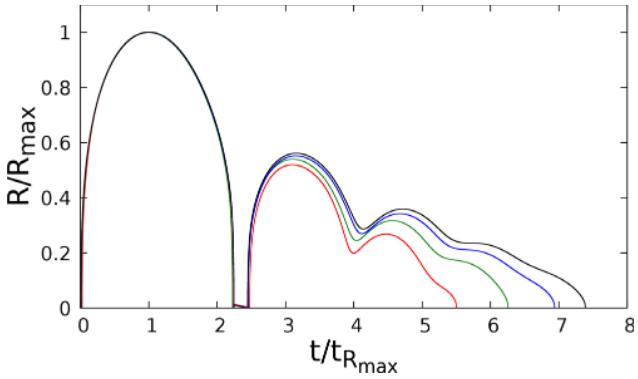

FIG. 1. Radius of the region delimited by the liquid/vapor interface $\rho = \rho_c$ vs time. The deposited energy $E_{Dep} = 8.9\times10^2$, 1.8×10^3, 2.8×10^3, 3.8×10^3 increases from red to black, at fixed $\rho_l = 2.15$. The graph is normalized with respect to the maximum bubble radius R_{max} and the time at which it is achieved $t = t_{R_{\max}}$.

In Fig. 2, the dynamics is illustrated through the density (a), energy (b), and radial velocity (c) fields selected during the first expansion phase ($t \le t_{R_{\max}}$), for a representative case. The motion of the initially homogeneous liquid at rest is triggered by the extra energy focused at the center of the domain, panel (b). This induces a sudden expansion and vaporizes the liquid producing the interface which encloses the vapor nucleus already visible at $t/t_{R_{\max}} = 0.05$, panel (a). Such abrupt expansion is accompanied by the emission of a (breakdown) shock wave that is launched in the liquid. In the meanwhile, the bubble grows until it gets to a maximum size (red solid lines in Fig. 2). At this point, the expansion stops and the velocity reverts to initiate the first collapse. During the process, the internal energy of the bubble is progressively transformed into kinetic energy and is mostly radiated away by the breakdown wave. This is reflected in the velocity profiles shown in Fig. 2(c).

The total energy of the system is composed of internal and kinetic energy, $E = U + K$, where U, in principle, consists of bulk and capillary contributions, Sec. II. In fact, the simulations show that capillarity does not substantially contribute to internal energy. During the expansion, the internal energy is transformed into kinetic energy, part of which is transferred to the surrounding liquid by the breakdown wave. Figure 3 provides the bubble's kinetic energy

$$K_b(t) = \int_0^{R(t)} \frac{1}{2}\rho u_r^2 4\pi r^2\, \mathrm{d}r \tag{11}$$

for a representative case. As in the classical Rayleigh–Plesset (RP)-like models, it vanishes when the bubble radius gets to R_{max}, at which point only internal energy is stored in the bubble. During the following collapse phase, $1 \le t/t_{R_{\max}} \le 2.3$, a part of the internal energy is transformed back to kinetic, which attains a relative maximum before getting to zero when the bubble disappears, see also Fig. 1.

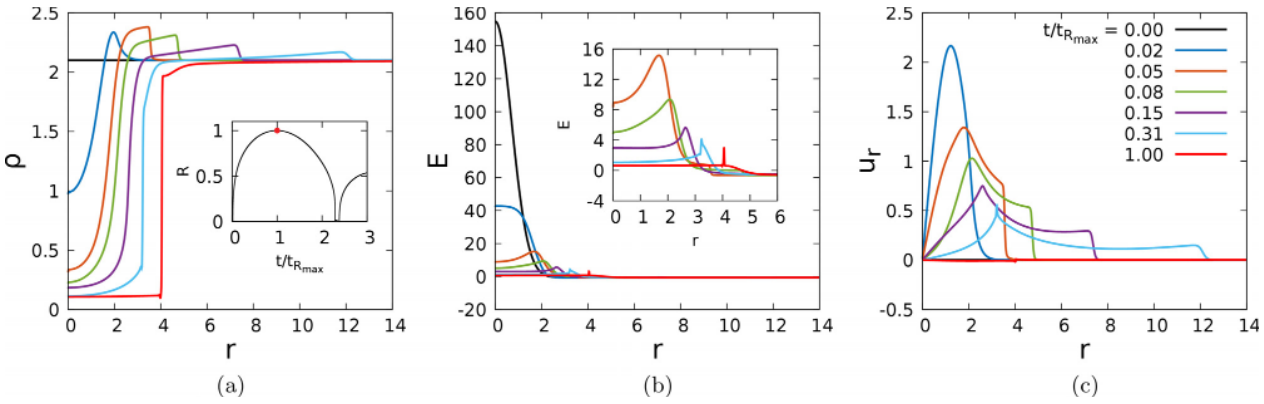

FIG. 2. Growth dynamics of a vapor bubble in terms of density (a), energy (b), and velocity (c) fields, for a case with $\rho_l = 2.1$ and $E_{Dep} = 865$. The times shown in panel (c) are normalized with $t_{R_{max}}$. In each panel, the solid red line represents the corresponding field when the bubble radius reaches R_{max}. The vapor bubble formation, together with the breakdown wave emission and propagation, is apparent in panel (a), with the inset showing the bubble radius vs time, the red dot highlighting R_{max}. The initial high-energy spot driving the dynamics, panel (b), is then partly transformed in kinetic energy and radiated away by the shock wave. The radial velocity field is provided in panel (c), where the velocity jump across the shock in the liquid is apparent for $t/t_{R_{max}} > 0.02$, and the peak radial velocity at each time instant can be roughly identified with the velocity of the liquid/vapor interface [see also panel (a)].

In laser-induced bubble experiments, the bubble potential energy at R_{max}[30–32] is evaluated as

$$E_{RP} = \left(p_l - p_v^{sat}(\theta_0)\right) V_b, \tag{12}$$

where p_l and $p_v^{sat}(\theta_0)$ are the unperturbed liquid pressure and the vapor saturation pressure at the initial temperature, respectively, with $V_b = 4/3\pi R_{\max}^3$ the maximum bubble volume. Equation (12) follows from the Rayleigh–Plesset (RP) model and holds for macroscopic bubbles.[49] This expression is inaccurate in the present case, given the bubble sizes of a few hundreds of nanometers, since the vapor pressure may deviate greatly from the saturation conditions.

The complete energy balance should also account for the energy radiated away by the breakdown shock wave, which can be computed as[50]

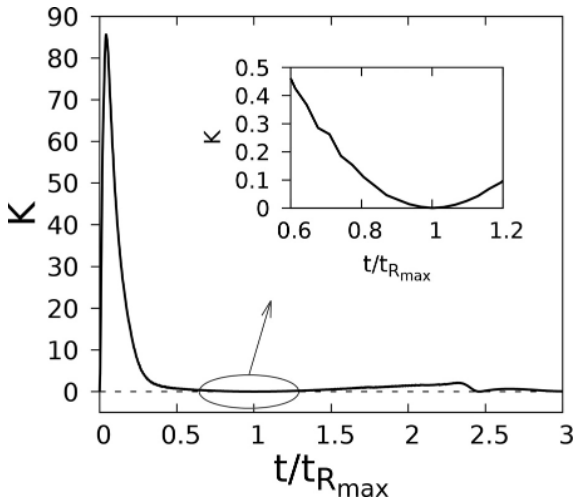

FIG. 3. Bubble kinetic energy vs time, computed as in (11), for a case with $\rho_l = 2.1$ and $E_{Dep} = 865$. The time interval close to maximum expansion is enlarged in the inset to show that the bubble kinetic energy approaches zero at $t = t_{R_{max}}$.

$$E_s = \frac{4\pi R_s^2}{\rho_l c_l} \int_0^{\tau} p_r(t)^2 \, \mathrm{d}t, \tag{13}$$

where R_s is the location where the relative pressure signal $p_r(t)$ is measured, and $c_l = \sqrt{32\theta/(3-\rho_l)^2 - 6\rho_l}$ is the local speed of sound for a van der Waals fluid.[51] Probes located at different radial positions R_s record the relative pressure with respect to the initial condition $p_r = p_0 - p_l$, Fig. 4, to allow computing E_s from Eq. (13).

Results gathered from 12 different numerical simulations, obtained varying ρ_l (E_0 as a consequence) and E_{Dep}, are presented in

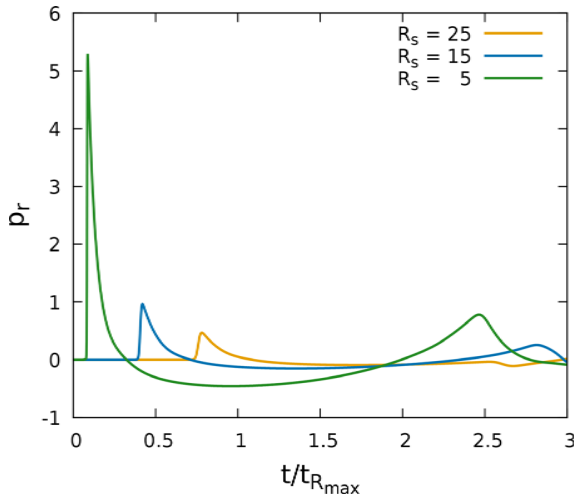

FIG. 4. Relative pressure profiles ($p_r = p_0 - p_l$) vs normalized time, measured at different radial distances R_s from the bubble center, for a case with $\rho_l = 2.1$ and $E_{Dep} = 865$. It is evident how the pressure signal gets attenuated as it travels within the liquid, as a result of the spherical propagation. The peaks visible at larger times are associated with the emission of shock wave during the collapse phase.

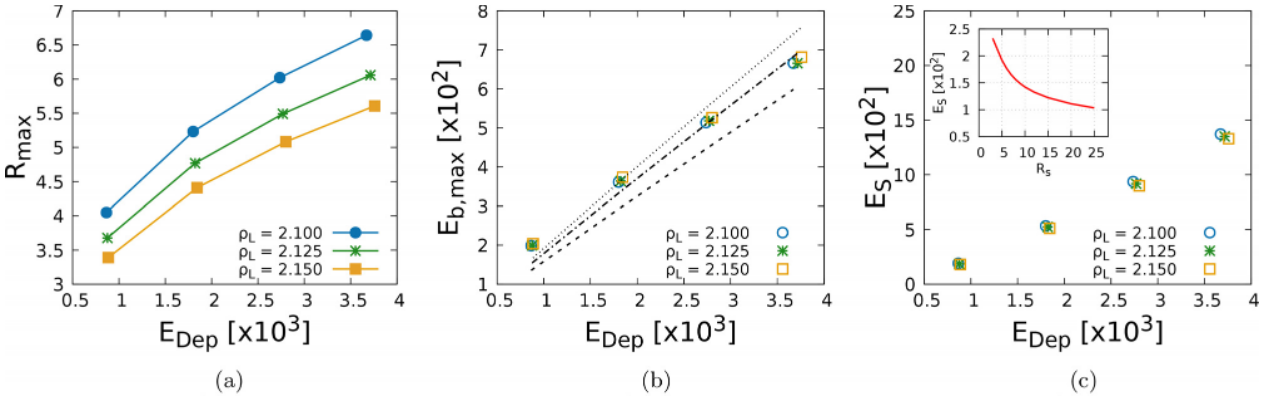

FIG. 5. Panel (a): maximum radius attained in the simulations during the first expansion stage vs E_{Dep}, for different initial densities (pressures) in the liquid. R_{max} increases with E_{Dep} and decreases with increasing ρ_l, because of the larger pressures in the liquid. Panel (b): bubble internal (total) energy at R_{max} vs E_{Dep}, linearly increasing with E_{Dep}, for different initial conditions. The lines represent values computed via Eq. (12) ($\rho_l = 2.1$ dashed, $\rho_l = 2.125$ dash-dotted, $\rho_l = 2.15$ dotted), showing how the RP prediction deviates from the actual internal energy of the bubble, depending on the initial condition. Panel (c): energy radiated by the breakdown wave, E_s, Eq. (13). In the inset, E_s vs R_s shows how the radiated energy is dissipated as the breakdown wave travels in the liquid, for the case with $\rho_l = 2.1$ and $E_{Dep} = 865$.

Fig. 5. Figure 5(a) shows the influence of the initial conditions on the maximum bubble radius, which obviously increases with the deposited laser energy, E_{Dep}, see, e.g., the experimental data in Ref. 32. An increase in the liquid density ρ_l reflects in an increase in the external initial liquid pressure p_l, such that the maximum radius attained during the expansion decreases for increasing ρ_l, because of the constraining action on the expanding bubble. The total energy of the bubble at R_{max} consists of the internal energy alone, which is shown in Fig. 5(b) together with the estimate provided by Eq. (12). The data depend linearly on E_{Dep} for all different ρ_l values, in agreement with experimental observations on macroscopic bubbles,[32,52] and the discrepancy between the numerical results and the potential energy estimate can be explained by noticing that for the time and length scales involved in the simulations, one cannot refer to a mechanical potential energy, since the system is not in static equilibrium, and non-equilibrium thermodynamics plays a preeminent role. The energy E_s radiated by the breakdown wave is plotted against E_{Dep} in Fig. 5(c) for different ρ_l, showing that the percentage of energy deposited that is transmitted to the liquid during the first expansion phase increases more than $E_{b,\max}$ for increasing E_{Dep}. The inset shows how the energy E_s is dissipated within the liquid as the breakdown wave passes through it.

All the results discussed so far have been obtained in the assumption of spherical symmetry, which is hardly achievable in experiments and applications.[53] In fact, recent experimental studies on laser-induced bubble cavitation report on the formation of non-spherical plasma shapes, and their importance on the subsequent bubble dynamics.[31,32] To better reproduce the actual dynamics of laser-induced bubbles, cylindrical axisymmetric simulations (see the Appendix), in which the initial energy deposition is non-spherical but rather elongated and constituted of different high-energy spots, can be performed. The initial density field is considered uniform, with $\rho(r, z, 0) = \rho_l = 2.1$, and the fluid is at rest, while the initial energy field mimics the elongated plasma configuration (see Figs. 5 in Ref. 31 and 4 in Ref. 32) with three Gaussian spots of different dimensions (variance) located at different heights on the axis of symmetry of the system. The subsequent dynamics are represented in Fig. 6 showing a pseudo-Schlieren field, namely, the exponential of minus the density gradient norm. This allows a neat visualization of the breakdown shock wave propagating in the liquid. The initial structure of the deposited energy is apparent. Subsequently, the three initially distinct spots coalesce to form a single vapor bubble which evolves to get almost spherical at larger times. A complex wave interaction pattern is also visible below the bubble, for $0.4 \leq t \leq 0.8$.

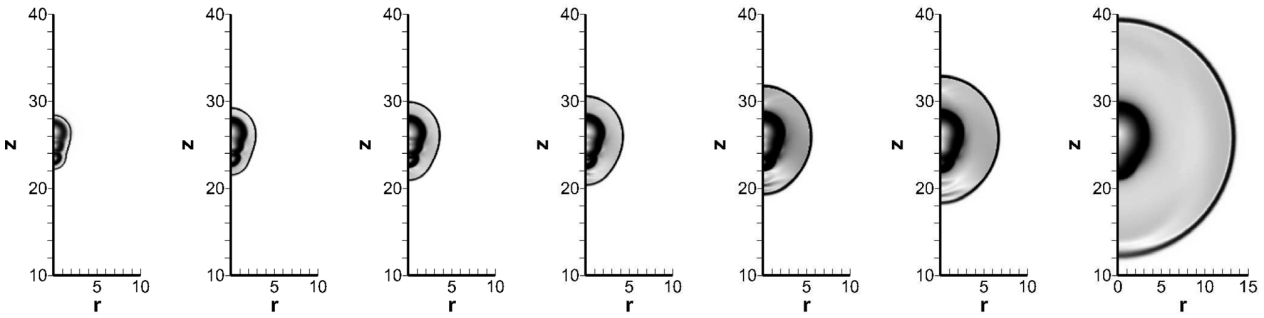

FIG. 6. Schlieren visualization of the bubble expansion with generated breakdown shock wave, for a cylindrical axisymmetric simulation with three Gaussian high-energy spots located at different heights. From left to right, dimensionless times $t = 0.1, 0.2, 0.3, 0.4, 0.6, 0.8, 2.1$.

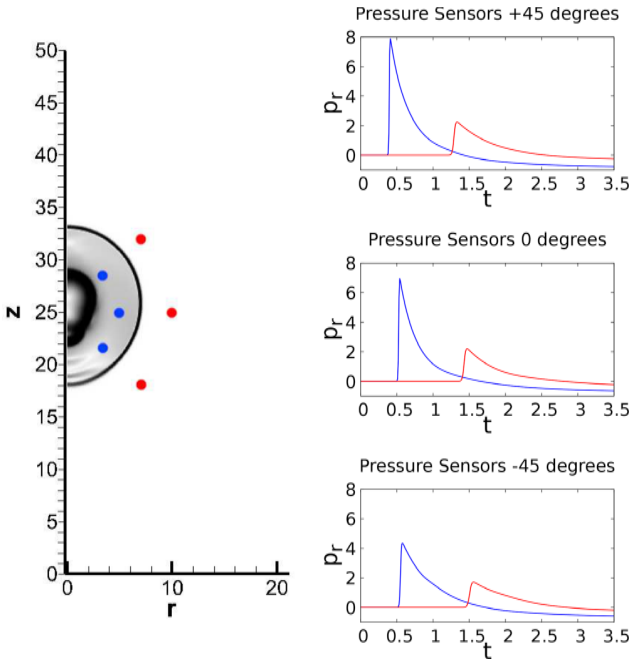

FIG. 7. On the left, first stages of the breakdown shock wave emission and propagation, with the probing locations where the relative pressure signals are measured in time. On the right, from top to bottom, the resulting pressure signals against time, for the probes located at +45°, 0°, and −45° with respect to the $\hat{\mathbf{r}}$ axis (counterclockwise).

To identify the profile of the pressure wave moving within the liquid phase, six different locations are probed, and the relative pressure in the liquid is computed as a function of time, Fig. 7. The asymmetries generated in the pressure field due to the initially non-spherical bubble configuration are clearly visible in the right panel, where pressure profiles measured at prescribed distances and angles relative to the initial high-energy spot are shown. Pressures are more intense near the top portion of the bubble (+45°), where the initial energy deposition is greater, and visibly less intense in the bottom portion (−45°), where the radius of deposition is smaller. These differences are more evident in the upstream (blue dots) than in the downstream (red dots) because in the latter the shock wave has already acquired an almost spherical symmetry (see also Fig. 6), a thing that is also apparent in the experiments, where initially elongated plasma formations turn into nearly spherical bubbles.

V. CONCLUSIONS

In this paper, a mesoscale approach based on a diffuse interface description of the liquid/vapor system is used to describe the phenomenon of laser-induced nano-/micro-cavitation bubbles. A van der Waals fluid model was used as a preliminary study to show the correct reproduction of the phenomenology of the process. In subsequent works, systems composed of water, e.g., using IAWPS EoS, can be investigated for the modeling of laser-induced nano-/microbubbles in real systems.

Spherically symmetric numerical simulations have been performed to gain insights on the peculiar dynamics of a single vapor bubble, from its initial nanoscopic formation into liquid, as a consequence of the high-energy deposition in a very narrow spot, to its hydrodynamic regime, characterized by a sequence of collapses and rebounds. The results show how the model is able to fully describe the system in terms of phase changes, transitions to supercritical states, and shock wave formation during both breakdown and collapse stages. The energies involved in the process and the related relevant fields have been analyzed, and the scaling of the bubble energy at maximum radius with respect to the energy deposited by the laser is found to be in agreement with experimental data available for macroscopic bubble evolution.[32,52] In this context, the discrepancy between the RP prediction for macroscopic bubbles, Eq. (12), and the results can be explained in light of the strong out of equilibrium conditions attained during nano-/microbubble dynamics.

Cylindrical axisymmetric simulations have shown the ability of the model to describe even non-spherical bubble formation and dynamics, a typical condition encountered in the experiments, where the focused laser beams generate elongated plasma shapes that affect the subsequent dynamics.

This study may lead to a better understanding of the energies involved in this process of formation, expansion, and subsequent collapse and rebounds of a single vapor bubble and may help in characterizing the dynamics of laser-induced nano- and micro-cavitation bubbles in its entirety.

ACKNOWLEDGMENTS

The support from the 2020 Sapienza Large Project: Dynamics of Biological and Artificial Lipid Bi-layer Membranes is greatly acknowledged. Concerning computational resources, we acknowledge PRACE for awarding us access to Marconi successor at CINECA, Italy, PRACE 23rd call Project No. 2021240074; DECI 17 SOLID project for resource Navigator based in Portugal at https://www.uc.pt/lca/ from the PRACE aisbl; CINECA award under the ISCRA initiative, for the availability of high-performance computing resources and support (ISCRA-B FHDAS). M.G. was financially supported by Leverhulme Trust Research Project Grant Amuse 2021.

AUTHOR DECLARATIONS

Conflict of Interest

The authors have no conflicts to disclose.

Author Contributions

Dario Abbondanza: Conceptualization (equal); Investigation (equal); Writing – original draft (lead); Writing – review & editing (lead). **Mirko Gallo:** Conceptualization (equal); Investigation (equal); Methodology (lead); Supervision (equal); Writing – original draft (supporting); Writing – review & editing (supporting). **Carlo Massimo Casciola:** Conceptualization (equal); Funding acquisition (lead); Project administration (lead); Supervision (lead); Writing – original draft (supporting); Writing – review & editing (supporting).

DATA AVAILABILITY

The data that support the findings of this study are available from the corresponding author upon reasonable request.

APPENDIX: EQUATIONS IN SPHERICAL AND CYLINDRICAL COORDINATES

Under spherical symmetry, the velocity vector is composed of the only radial component

$$\mathbf{u}(r,\theta,\varphi) = u_r(r)\hat{\mathbf{r}}, \tag{A1}$$

which is a function of the only radial coordinate. The system of equations (3) then takes the form

$$\frac{\partial \rho}{\partial t} + \frac{1}{r^2}\frac{\partial (r^2 \rho u_r)}{\partial r} = 0, \tag{A2}$$

$$\frac{\partial (\rho u_r)}{\partial t} + \frac{1}{r^2}\frac{\partial \left[r^2(\rho u_r^2 - T_{rr})\right]}{\partial r} + \frac{(T_{\theta\theta} + T_{\varphi\varphi})}{r} = 0, \tag{A3}$$

$$\frac{\partial E}{\partial t} + \frac{1}{r^2}\frac{\partial}{\partial r}\left[r^2(Eu_r - T_{rr}u_r + q_e)\right] = 0, \tag{A4}$$

where the stress tensor T has the structure

$$T = T_{rr}\,\hat{\mathbf{r}} \otimes \hat{\mathbf{r}} + T_{\theta\theta}\,\hat{\boldsymbol{\theta}} \otimes \hat{\boldsymbol{\theta}} + T_{\varphi\varphi}\,\hat{\boldsymbol{\varphi}} \otimes \hat{\boldsymbol{\varphi}}, \tag{A5}$$

with components

$$T_{rr} = -p + \lambda\left[-\frac{1}{2}\left(\frac{\partial \rho^2}{\partial r}\right) + \frac{\rho}{r^2}\frac{\partial}{\partial r}\left(r^2\frac{\partial \rho}{\partial r}\right)\right] + 2\mu\left[\frac{\partial u_r}{\partial r} - \frac{1}{3r^2}\frac{\partial (r^2 u_r)}{\partial r}\right], \tag{A6}$$

$$T_{\theta\theta} = T_{\varphi\varphi} = -p + \lambda\left[\frac{1}{2}\left(\frac{\partial \rho^2}{\partial r}\right) + \frac{\rho}{r^2}\frac{\partial}{\partial r}\left(r^2\frac{\partial \rho}{\partial r}\right)\right] + 2\mu\left[\frac{u_r}{r} - \frac{1}{3r^2}\frac{\partial (r^2 u_r)}{\partial r}\right], \tag{A7}$$

and the energy flux q_e takes the form

$$q_e = -k\frac{\partial \theta}{\partial r} + \frac{\lambda\rho}{r^2}\frac{\partial \rho}{\partial r}\frac{\partial (r^2 u_r)}{\partial r}. \tag{A8}$$

Under axial symmetry, the velocity is

$$\mathbf{u}(r,\theta,z) = u_r(r,z)\hat{\mathbf{r}} + u_z(r,z)\hat{\mathbf{z}}, \tag{A9}$$

with radial and axial components depending on the radial and axial coordinates. The system of equations (3) then reads

$$\frac{\partial \rho}{\partial t} + \frac{1}{r}\frac{\partial (r\rho u_r)}{\partial r} + \frac{\partial (\rho u_z)}{\partial z} = 0, \tag{A10}$$

$$\frac{\partial (\rho u_r)}{\partial t} + \frac{1}{r}\frac{\partial (r\rho u_r^2)}{\partial r} + \frac{\partial (\rho u_r u_z)}{\partial z} = \frac{1}{r}\frac{\partial (rT_{rr})}{\partial r} + \frac{\partial T_{rz}}{\partial z} - \frac{T_{\theta\theta}}{r}, \tag{A11}$$

$$\frac{\partial (\rho u_z)}{\partial t} + \frac{\partial (\rho u_z^2)}{\partial z} + \frac{1}{r}\frac{\partial (r\rho u_r u_z)}{\partial r} = \frac{\partial T_{zz}}{\partial z} + \frac{1}{r}\frac{\partial r T_{rz}}{\partial r}, \tag{A12}$$

$$\frac{\partial E}{\partial t} + \frac{1}{r}\frac{\partial}{\partial r}\left[r\left(Eu_r - T_{rr}u_r - T_{rz}u_z + q_e^r\right)\right] + \frac{\partial}{\partial z}\left[Eu_z - T_{zr}u_r - T_{zz}u_z + q_e^z\right] = 0, \tag{A13}$$

where the stress tensor T has the structure (symmetric rank-2 tensor)

$$T = T_{rr}\,\hat{\mathbf{r}} \otimes \hat{\mathbf{r}} + T_{rz}\,(\hat{\mathbf{r}} \otimes \hat{\mathbf{z}} + \hat{\mathbf{z}} \otimes \hat{\mathbf{r}}) + T_{zz}\,\hat{\mathbf{z}} \otimes \hat{\mathbf{z}} + T_{\theta\theta}\,\hat{\boldsymbol{\theta}} \otimes \hat{\boldsymbol{\theta}}, \tag{A14}$$

with components

$$T_{rr} = -p + \frac{\lambda}{2}\left[-\left(\frac{\partial \rho}{\partial r}\right)^2 + \left(\frac{\partial \rho}{\partial z}\right)^2\right] + \frac{\rho\lambda}{r}\left[\frac{\partial}{\partial r}\left(r\frac{\partial \rho}{\partial r}\right) + r\frac{\partial^2 \rho}{\partial z^2}\right] - \frac{2}{3}\mu\left(\frac{1}{r}\frac{\partial (ru_r)}{\partial r} + \frac{\partial u_z}{\partial z}\right) + 2\mu\frac{\partial u_r}{\partial r},$$

$$T_{zz} = -p + \frac{\lambda}{2}\left[\left(\frac{\partial \rho}{\partial r}\right)^2 - \left(\frac{\partial \rho}{\partial z}\right)^2\right] + \frac{\rho\lambda}{r}\left[\frac{\partial}{\partial r}\left(r\frac{\partial \rho}{\partial r}\right) + r\frac{\partial^2 \rho}{\partial z^2}\right] - \frac{2}{3}\mu\left(\frac{1}{r}\frac{\partial (ru_r)}{\partial r} + \frac{\partial u_z}{\partial z}\right) + 2\mu\frac{\partial u_z}{\partial z}, \tag{A15}$$

$$T_{rz} = -\lambda\frac{\partial \rho}{\partial r}\frac{\partial \rho}{\partial z} + \mu\left(\frac{\partial u_r}{\partial z} + \frac{\partial u_z}{\partial r}\right),$$

$$T_{\theta\theta} = -p + \frac{\lambda}{2}\left[\left(\frac{\partial \rho}{\partial r}\right)^2 + \left(\frac{\partial \rho}{\partial z}\right)^2\right] + \frac{\rho\lambda}{r}\left[\frac{\partial}{\partial r}\left(r\frac{\partial \rho}{\partial r}\right) + r\frac{\partial^2 \rho}{\partial z^2}\right] - \frac{2}{3}\mu\left(\frac{1}{r}\frac{\partial (ru_r)}{\partial r} + \frac{\partial u_z}{\partial z}\right) + 2\mu\frac{u_r}{r},$$

while the two components of the energy flux $\mathbf{q}_e = q_e^r\,\hat{\mathbf{r}} + q_e^z\,\hat{\mathbf{z}}$ are

$$q_e^r = -k\frac{\partial \theta}{\partial r} + \lambda\rho\frac{\partial \rho}{\partial r}\left(\frac{1}{r}\frac{\partial (ru_r)}{\partial r} + \frac{\partial u_z}{\partial z}\right), \tag{A16}$$

$$q_e^z = -k\frac{\partial \theta}{\partial z} + \lambda\rho\frac{\partial \rho}{\partial z}\left(\frac{1}{r}\frac{\partial (ru_r)}{\partial r} + \frac{\partial u_z}{\partial z}\right). \tag{A17}$$

REFERENCES

[1] D. J. Flannigan and K. S. Suslick, "Plasma formation and temperature measurement during single-bubble cavitation," Nature **434**, 52 (2005).
[2] C.-D. Ohl, A. Philipp, and W. Lauterborn, "Cavitation bubble collapse studied at 20 million frames per second," Ann. Phys. **507**, 26 (1995).
[3] J. R. Blake and D. Gibson, "Cavitation bubbles near boundaries," Annu. Rev. Fluid Mech. **19**, 99 (1987).
[4] T. B. Benjamin and A. T. Ellis, "A discussion on deformation of solids by the impact of liquids, and its relation to rain damage in aircraft and missiles, to blade erosion in steam turbines, and to cavitation erosion - The collapse of cavitation bubbles and the pressures thereby produced against solid boundaries," Philos. Trans. R. Soc. London, Ser. A **260**, 221 (1966).
[5] M. Plesset and A. Ellis, "On the mechanism of cavitation damage," Trans. ASME **77**, 1055 (1955).
[6] D. Abbondanza, M. Gallo, and C. M. Casciola, "Cavitation over solid surfaces: microbubble collapse, shock waves, and elastic response," Meccanica (published online) (2022).
[7] G. Silvani, C. Scognamiglio, D. Caprini, L. Marino, M. Chinappi, G. Sinibaldi, G. Peruzzi, M. F. Kiani, and C. M. Casciola, "Reversible cavitation-induced junctional opening in an artificial endothelial layer," Small **15**, 1905375 (2019).
[8] G. Grisanti, D. Caprini, G. Sinibaldi, C. Scognamiglio, G. Silvani, G. Peruzzi, and C. M. Casciola, "A microfluidic platform for cavitation-enhanced drug delivery," Micromachines **12**, 658 (2021).
[9] S. Zhu, F. H. Cocks, G. M. Preminger, and P. Zhong, "The role of stress waves and cavitation in stone comminution in shock wave lithotripsy," Ultrasound Med. Biol. **28**, 661 (2002).
[10] A. Vogel, P. Schweiger, A. Frieser, M. N. Asiyo, and R. Birngruber, "Intraocular Nd:YAG laser surgery: Laser-tissue interaction, damage range, and reduction of collateral effects," IEEE J. Quantum Electron. **26**, 2240 (1990).
[11] T. Juhasz, F. H. Loesel, R. M. Kurtz, C. Horvath, J. F. Bille, and G. Mourou, "Corneal refractive surgery with femtosecond lasers," IEEE J. Sel. Top. Quantum Electron. **5**, 902 (1999).

[12]F. Sauvage, V. P. Nguyen, Y. Li, A. Harizaj, J. Sebag, D. Roels, V. Van Havere, K. Peynshaert, R. Xiong, J. C. Fraire *et al.*, "Laser-induced nanobubbles safely ablate vitreous opacities in vivo," Nat. Nanotechnol. **17**, 552 (2022).
[13]X. Noblin, N. Rojas, J. Westbrook, C. Llorens, M. Argentina, and J. Dumais, "The fern sporangium: A unique catapult," Science **335**, 1322 (2012).
[14]C. Scognamiglio, F. Magaletti, Y. Izmaylov, M. Gallo, C. M. Casciola, and X. Noblin, "The detailed acoustic signature of a micro-confined cavitation bubble," Soft Matter **14**, 7987 (2018).
[15]A. Vogel, N. Linz, S. Freidank, and G. Paltauf, "Femtosecond-laser-induced nanocavitation in water: Implications for optical breakdown threshold and cell surgery," Phys. Rev. Lett. **100**, 038102 (2008).
[16]L. Rayleigh, "On the pressure developed in a liquid during the collapse of a spherical cavity," London Edinburgh Dublin Philos. Mag. J. Sci. **34**, 94 (1917).
[17]M. S. Plesset and A. Prosperetti, "Bubble dynamics and cavitation," Annu. Rev. Fluid Mech. **9**, 145 (1977).
[18]F. Magaletti, M. Gallo, and C. M. Casciola, "Water cavitation from ambient to high temperatures," Sci. Rep. **11**, 20801 (2021).
[19]E. Benilov, "Asymptotic reductions of the diffuse-interface model with applications to contact lines in fluids," Phys. Rev. Fluids **5**, 084003 (2020).
[20]F. Caupin, "Liquid-vapor interface, cavitation, and the phase diagram of water," Phys. Rev. E **71**, 051605 (2005).
[21]J. Diemand, R. Angélil, K. K. Tanaka, and H. Tanaka, "Large scale molecular dynamics simulations of homogeneous nucleation," J. Chem. Phys. **139**, 074309 (2013).
[22]G. Menzl, M. A. Gonzalez, P. Geiger, F. Caupin, J. L. Abascal, C. Valeriani, and C. Dellago, "Molecular mechanism for cavitation in water under tension," Proc. Natl. Acad. Sci. **113**, 13582 (2016).
[23]M. Gallo, F. Magaletti, and C. M. Casciola, "Fluctuating hydrodynamics as a tool to investigate nucleation of cavitation bubbles," Int. J. Comput. Methods Exp. **6**(2), 345–357 (2018).
[24]M. Gallo, F. Magaletti, and C. M. Casciola, "Thermally activated vapor bubble nucleation: The Landau-Lifshitz–Van der Waals approach," Phys. Rev. Fluids **3**, 053604 (2018).
[25]M. Gallo, F. Magaletti, D. Cocco, and C. M. Casciola, "Nucleation and growth dynamics of vapour bubbles," J. Fluid Mech. **883**, A14 (2020).
[26]M. Gallo, F. Magaletti, and C. M. Casciola, "Heterogeneous bubble nucleation dynamics," J. Fluid Mech. **906**, A20 (2021).
[27]F. Magaletti, L. Marino, and C. Casciola, "Shock wave formation in the collapse of a vapor nanobubble," Phys. Rev. Lett. **114**, 064501 (2015).
[28]F. Magaletti, M. Gallo, L. Marino, and C. M. Casciola, "Shock-induced collapse of a vapor nanobubble near solid boundaries," Int. J. Multiphase Flow **84**, 34 (2016).
[29]F. Magaletti, M. Gallo, L. Marino, and C. M. Casciola, "Dynamics of a vapor nanobubble collapsing near a solid boundary," J. Phys.: Conf. Ser. **656**, 012012 (2015).
[30]A. Vogel, J. Noack, K. Nahen, D. Theisen, S. Busch, U. Parlitz, D. Hammer, G. Noojin, B. Rockwell, and R. Birngruber, "Energy balance of optical breakdown in water at nanosecond to femtosecond time scales," Appl. Phys. B: Lasers Opt. **68**, 271 (1999).
[31]X.-X. Liang, N. Linz, S. Freidank, G. Paltauf, and A. Vogel, "Comprehensive analysis of spherical bubble oscillations and shock wave emission in laser-induced cavitation," J. Fluid Mech. **940**, A5 (2022).
[32]G. Sinibaldi, A. Occhicone, F. Alves Pereira, D. Caprini, L. Marino, F. Michelotti, and C. Casciola, "Laser induced cavitation: Plasma generation and breakdown shockwave," Phys. Fluids **31**, 103302 (2019).
[33]B. R. Novak, E. J. Maginn, and M. J. McCready, "Comparison of heterogeneous and homogeneous bubble nucleation using molecular simulations," Phys. Rev. B **75**, 085413 (2007).
[34]J. Diemand, R. Angélil, K. K. Tanaka, and H. Tanaka, "Direct simulations of homogeneous bubble nucleation: Agreement with classical nucleation theory and no local hot spots," Phys. Rev. E **90**, 052407 (2014).
[35]P. C. Hohenberg and B. I. Halperin, "Theory of dynamic critical phenomena," Rev. Mod. Phys. **49**, 435 (1977).
[36]D. Anderson, G. McFadden, and A. Wheeler, "Diffuse-interface methods in fluid mechanics," Annu. Rev. Fluid Mech. **30**, 139 (1998).
[37]J. F. Lutsko, "Density functional theory of inhomogeneous liquids. IV. Squared-gradient approximation and classical nucleation theory," J. Chem. Phys. **134**, 164501 (2011).
[38]Ø. Wilhelmsen, T. T. Trinh, S. Kjelstrup, and D. Bedeaux, "Influence of curvature on the transfer coefficients for evaporation and condensation of Lennard-Jones fluid from square-gradient theory and nonequilibrium molecular dynamics," J. Phys. Chem. C **119**, 8160 (2015).
[39]E. Benilov, "Can a liquid drop on a substrate be in equilibrium with saturated vapor?," Phys. Rev. E **104**, L032103 (2021).
[40]E. Benilov, "Capillary condensation of saturated vapor in a corner formed by two intersecting walls," Phys. Fluids **34**, 062103 (2022).
[41]G. R. Lázaro, I. Pagonabarraga, and A. Hernández-Machado, "Phase-field theories for mathematical modeling of biological membranes," Chem. Phys. Lipids **185**, 46 (2015).
[42]M. Bottacchiari, M. Gallo, M. Bussoletti, and C. M. Casciola, "Activation energy and force fields during topological transitions of fluid lipid vesicles," Commun. Phys. **5**, 283 (2022).
[43]J. D. Van der Waals, "The thermodynamic theory of capillarity under the hypothesis of a continuous variation of density," J. Stat. Phys. **20**, 200 (1979).
[44]D. Jamet, O. Lebaigue, N. Coutris, and J. Delhaye, "The second gradient method for the direct numerical simulation of liquid–vapor flows with phase change," J. Comput. Phys. **169**, 624 (2001).
[45]A. Chaudhri, J. B. Bell, A. L. Garcia, and A. Donev, "Modeling multiphase flow using fluctuating hydrodynamics," Phys. Rev. E **90**, 033014 (2014).
[46]F. Magaletti, M. Gallo, S. P. Perez, J. A. Carrillo, and S. Kalliadasis, "A positivity-preserving scheme for fluctuating hydrodynamics," J. Comput. Phys. **463**, 111248 (2022).
[47]M. Gallo, "Thermal fluctuations in metastable fluids," Phys. Fluids **34**, 122011 (2022).
[48]S. R. De Groot and P. Mazur, *Non-Equilibrium Thermodynamics* (Courier Dover Publications, 2013).
[49]C. E. Brennen, *Cavitation and Bubble Dynamics* (Cambridge University Press, 2014).
[50]R. H. Cole and R. Weller, "Underwater explosions," Phys. Today **1**(6), 35 (1948).
[51]N. Zhao, A. Mentrelli, T. Ruggeri, and M. Sugiyama, "Admissible shock waves and shock-induced phase transitions in a van der Waals fluid," Phys. Fluids **23**, 086101 (2011).
[52]W. Lauterborn and A. Vogel, *Bubble Dynamics and Shock Waves* (Springer, 2013), pp. 67–103.
[53]D. Obreschkow, M. Tinguely, N. Dorsaz, P. Kobel, A. De Bosset, and M. Farhat, "The quest for the most spherical bubble: Experimental setup and data overview," Exp. Fluids **54**, 1503 (2013).